Upscaled models of flow and transport in faulted sandstone: boundary condition effects and explicit fracture modelling

Eric A. Flodin[1, 2], Louis J. Durlofsky[3, 4] and Atilla Aydin[1]

[1]*Department of Geological and Environmental Sciences, Stanford University, Stanford, CA 94305-2115, USA*
[2]*Present address: ChevronTexaco Energy Technology Company, PO Box 6019, San Ramon, CA 94583-0719, USA (e-mail: eflodin@chevrontexaco.com)*
[3]*Department of Petroleum Engineering, Stanford University, Stanford, CA 94305-2220, USA*
[4]*ChevronTexaco Energy Technology Company, PO Box 6019, San Ramon, CA 94583-0719, USA*

ABSTRACT: Faults formed by shearing of joint zones in sandstone contain fine-scale features that cannot be represented explicitly in large-scale flow simulations. Upscaled models are, therefore, required for reservoir engineering computations. These models attempt to capture fine-scale effects through equivalent permeabilities that are computed from the underlying fine-scale characterization. In this paper the impact of several different local boundary conditions on the calculated equivalent permeability is assessed. Pressure–no-flow, periodic and mirror-periodic boundary specifications are considered. The resulting coarse-scale permeability tensors are shown to be highly dependent on the local boundary conditions used in the models. In cases with through-going high-permeability features, pressure–no-flow and mirror-periodic boundary conditions provide upscaled permeabilities that correctly capture global flow characteristics. Periodic boundary conditions, by contrast, are more suitable for systems lacking through-going high-permeability features. This sensitivity to boundary conditions calls into question the robustness of the equivalent permeability for the general case and suggests that dominant through-going features would best be modelled explicitly. In addition, due to the very small thickness and high permeability of some through-going structural features (e.g. slip surfaces), globally upscaled models are inadequate for the modelling of transport. To address these issues, a 'partial upscaling' method – removing the through-going high-permeability features from the fine model, upscaling to a coarse grid and then reintroducing the high-permeability features back into the coarsened model – is adopted. This procedure is shown to provide coarse models that give accurate predictions for both flow and transport.

KEYWORDS: *faults, fractures, permeability, upscaling, boundary conditions*

INTRODUCTION

Recent outcrop-based characterizations of fault zones systematically describe features down to the millimetre-scale (Myers 1999; Myers & Aydin 2004). Before these highly detailed models can be used for flow simulations, some type of coarsening or upscaling procedure must be applied. The goal of upscaling is to replace the fine-scale model with a coarsened model that preserves the flow and transport properties of the fine model. A variety of upscaling methodologies exist, including both numerical flow simulation techniques (e.g. Durlofsky 1991; Pickup *et al.* 1994) and analytical or power averaging approaches (e.g. Deutsch 1989). Thorough reviews of various upscaling methodologies can be found in Wen & Gomez-Hernandez (1996) and Renard & de Marsily (1997).

In this paper, a finite-difference solution of the local single-phase flow equation is used to calculate upscaled permeability tensors. This work builds on a recent study (Jourde *et al.* 2002) and further explores the effects of boundary conditions on upscaled fault permeabilities. Toward this goal, a number of different boundary specifications, namely pressure–no-flow, periodic, and mirror-periodic conditions, are considered. The appropriate boundary condition is shown to depend mainly on the degree of large-scale connectivity of the dominant high-permeability features. This suggests that the upscaling of certain types of through-going features (e.g. slip surfaces and joints that are longer than the block dimensions) does not, in general, provide robust coarse-scale models.

To circumvent this difficulty, a modified upscaling procedure is described. In this approach, which shares some similarities with earlier techniques (e.g. Durlofsky *et al.* 1997; Lee *et al.* 2001), the dominant through-going features are first removed and the remaining 'background' heterogeneities are then upscaled. This upscaling is much less sensitive to the boundary conditions since the dominant features are no longer homogenized. These features are, however, reintroduced into the coarse-scale model, where they are represented explicitly. This procedure is shown to provide accurate and robust coarse-scale

1354-0793/04/$15.00

models for both flow and transport through blocks that include a fault zone.

A number of previous investigators developed techniques for estimating the large-scale flow properties of fault zones. For example, Shipton *et al.* (2002) calculated upscaled permeabilities by applying power averaging techniques to structural data acquired from sample core. Caine & Forster (1999) computed large-scale permeabilities for a number of stochastically generated brittle fault zones embedded within low permeability matrix. Walsh *et al.* (1998) and Manzocchi *et al.* (1999) developed correlations for fault thickness and cross-fault permeability, which can be used to compute cross-fault transmissibility for use in flow simulators. In more recent papers, Harris *et al.* (2002) applied the methods to a particular case study in the North Sea and Manzocchi *et al.* (2002) extended these approaches to address the effects of two-phase flow. A large number of studies have addressed the calculation of the effective permeability of fractured systems. Recent work within the context of reservoir simulation includes the studies of Nakashima *et al.* (2000), Lee *et al.* (2001), Couples *et al.* (2003) and references therein. The work described here differs from previous studies in that it begins with highly detailed outcrop characterizations. From these descriptions, coarse simulation models are generated to describe flow in the fault zone and the impact of various boundary conditions on the accuracy of these models is tested. In addition, transport through the fault zone is considered and the difficult problem of accurately capturing fault-parallel displacements in coarse models is addressed.

The paper proceeds as follows. The governing equations and the various boundary conditions to be tested for upscaling are described first. A simple, idealized permeability field is then considered and equivalent permeabilities are computed using the different boundary conditions. The boundary conditions are then applied to more complicated permeability fields that occur in the vicinity of a fault. The use of power averaging for representing the overall fault zone permeability for a range of fault slips is briefly considered. The paper then describes the modified upscaling procedure in which the dominant through-going features of the fault zone are explicitly represented while the remaining elements of the fault zone are upscaled. The efficacy of this procedure is demonstrated using a detailed fault zone model.

FLOW EQUATIONS AND BOUNDARY CONDITIONS

Single-phase, steady-state incompressible flow through a porous medium is described by Darcy's law and the continuity equation:

$$\mathbf{u} = -\frac{1}{\mu}\mathbf{k}\cdot\nabla p, \tag{1}$$

$$\nabla\cdot\mathbf{u} = 0, \tag{2}$$

where $\mathbf{u}$ is the Darcy velocity vector, p is pressure, μ is the fluid viscosity, and $\mathbf{k}$ is the permeability tensor. Equations (1) and (2) are used to model flow for both the fine and coarse scales, though for the coarse-scale the equivalent or upscaled permeability tensor, $\mathbf{k}^*$, replaces the fine-scale permeability, $\mathbf{k}$. In this work, the coarse-scale permeability is computed from the underlying fine-scale description by solving a local fine-scale problem. This local problem involves the region of the fine-scale model corresponding to a single coarse-scale block. To determine $\mathbf{k}^*$ from this local solution, equations (1) and (2) are solved over the local domain and the fine-scale results are post-processed as described below. In some cases, $\mathbf{k}^*$ is computed over the entire fine-scale region. This corresponds to upscaling the fine-scale description of the fault zone to a single coarse block.

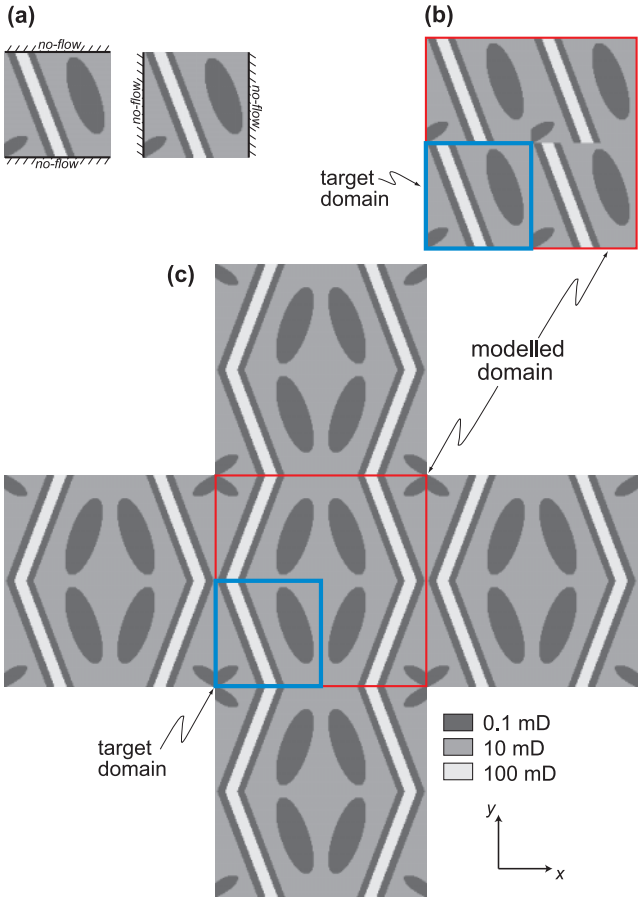

Fig. 1. Boundary condition examples. (**a**) Pressure–no-flow boundary condition. (**b**) Periodic boundary conditions. (**c**) Mirror-periodic boundary conditions.

In the numerical computations a standard finite-difference method is applied, with intercell transmissibilities computed via weighted harmonic averages. The different boundary conditions and post-processing procedures used to compute the upscaled permeabilities are now described. One should note that upscaling methods that apply global flow information also exist (e.g. Holden & Nielsen 2000; Chen *et al.* 2003) and may be suitable for the problem under study, though no such methods were investigated in this work.

Pressure–no-flow boundary conditions

The simplest boundary condition that is applied is that of pressure–no-flow (Fig. 1a). The flow problem is solved first in the x-direction and then in the y-direction. In the case of the x-direction solution, the pressure is prescribed as p=1 on the left edge and p=0 on the right edge, with no-flow conditions on the other two boundaries. The opposite scenario is used to solve for flow in the y-direction. The equivalent permeability, $\mathbf{k}^*$, is calculated from these two solutions. Choosing the x- and y-axes to align with the principal directions of the permeability tensor (i.e. neglecting the cross-terms k^*_{xy} and k^*_{yx}), the k^*_{xx} component can be computed using the following relationship:

$$k^*_{xx} = \frac{Q_x \mu L_x}{L_y \Delta p} \tag{3}$$

where Qx is the total flow-rate through the system computed at the outlet edge, Lx and Ly are the system dimensions, and Δp is the pressure difference in the x-direction. The k^*_{yy} component is obtained using a variant of equation (3), with the pressure difference and total flow now in the y-direction. Note that this method applies outlet averaging to compute $\mathbf{k}^*$ from the fine-scale solution. This was the method used to calculate $\mathbf{k}^*$ for the fault zones studied by Jourde *et al.* (2002).

When the principal directions of permeability are unknown, a more general approach for the determination of $\mathbf{k}^*$ is required. In this case the outlet average described above is inadequate since the permeability cross-terms are assumed to be zero. Pressure–no-flow boundary conditions can still be used, but the full tensor, $\mathbf{k}^*$, must be computed using a modified procedure for the post-processing of the two sets of fine-scale results. Specifically, one applies the following relationship (Wu *et al.* 2002; Wen *et al.* 2003) to determine $\mathbf{k}^*$:

$$\langle \mathbf{u} \rangle = -\frac{1}{\mu}\mathbf{k}^* \cdot \langle \nabla p \rangle, \tag{4}$$

where $\langle u \rangle$ and $\langle \nabla p \rangle$ are area (in two dimensions) or volume (in three dimensions) averaged Darcy velocity and pressure gradient. In two dimensions, there are four components of $\mathbf{k}^*$ to be determined. Equation (4) represents four equations because two fine grid problems are solved and each involves two components of $\langle \mathbf{u} \rangle$ and $\langle \nabla p \rangle$. Thus, the system is fully specified. Symmetry for $\mathbf{k}^*$ can be enforced in several different ways. The simplest approach is to set the cross-terms equal to the average of the computed k^*_{xy} and k^*_{yx}. An alternative procedure that enforces symmetry via a least-square approach is described in Wen *et al.* (2003).

Periodic boundary conditions

Periodic boundary conditions represent the region of interest as though it were infinitely repeated over the modelling domain. A portion of the periodic repetition of the permeability field referred to above is illustrated in Figure 1b. Periodic boundary conditions equate flow on one side of the domain to that on the opposite side of the domain. Specifically, one sets $u_x(x{=}0,y){=}u_x(x{=}L_x,y)$ and $u_y(x,y{=}0){=}u_y(x,y{=}L_y)$. Boundary pressures are specified to contain similar correspondences, though a jump, which drives the global flow, is prescribed in each of the coordinate directions in turn. The upscaled permeability tensor, $\mathbf{k}^*$, is then computed from the local fine grid solutions using equation (4). Due to the properties of periodic boundary conditions, the identical $\mathbf{k}^*$ can also be computed using the outlet average information. See Durlofsky (1991), Pickup *et al.* (1994) and Wen *et al.* (2003) for further details on periodic boundary conditions, as well as Lee *et al.* (2001) and Nakashima *et al.* (2000) for their application in the upscaling of fractured systems.

Mirror-periodic boundary conditions

As can be seen below, periodic boundary conditions can act to break the connectivity of large-scale permeability features (Fig. 1b). Alternative boundary conditions can be applied in an attempt to maintain this connectivity. Here, the paper considers a mirroring procedure in which the local domain of interest is reflected around each of its four edges (in two dimensions) (Fig. 1c). If this process is repeated, a periodic domain containing the original model plus its reflections is generated. This procedure ensures the connectivity of large-scale features, but their orientations are distorted in the replicated domains. This type of approach was taken by Martys *et al.* (1999) in flow simulations of three-dimensional pore space models in order to enforce pore connectivity across the domain boundaries.

Mirror-periodic boundary conditions are applied here by first reflecting the domain in the y-direction and then reflecting this 'doubled domain' again in the x-direction (Fig. 1c). Periodic boundary conditions are then applied to the extended domain (red box, Fig. 1c). A portion of the periodic repetition of this mirrored domain is shown in Figure 1c.

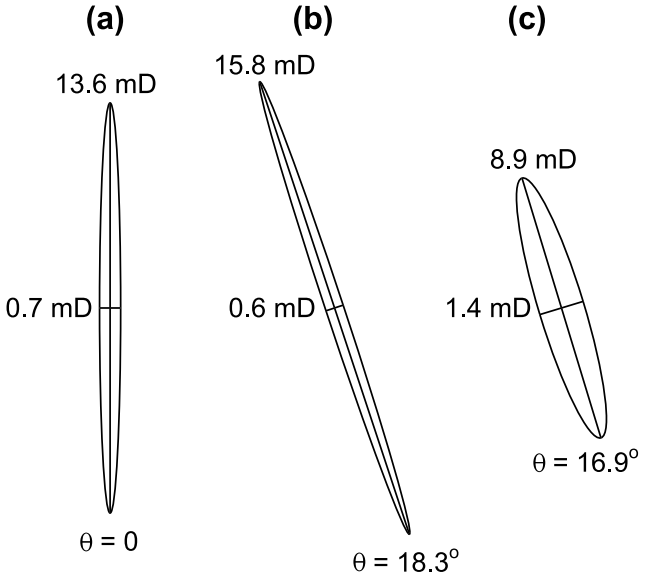

Fig. 2. Permeability tensors for the permeability field shown in Figure 1 calculated using the various boundary conditions. (**a**) Outlet averaged pressure – no-flow, and area averaged mirror-periodic boundary condition results. (**b**) Area averaged pressure – no-flow and target domain mirror-periodic boundary condition results. (**c**) Periodic boundary condition results.

COMPARISON OF BOUNDARY CONDITIONS FOR AN IDEALIZED SYSTEM

Ideally, the computed $\mathbf{k}^*$ for a given permeability field should be nearly the same regardless of the boundary conditions used for upscaling. In practice, however, upscaled permeabilities computed for heterogeneous permeability fields display some degree of dependence on the assumed boundary conditions. In many cases this dependence is not practically significant, even though quantitative differences between the resulting upscaled permeabilities might be evident. In other cases, for example in calculations involving flow in a fault zone, the assumed boundary conditions can have a large effect on the upscaled description.

As an example of the variation in $\mathbf{k}^*$ computed with different boundary conditions, the permeability field shown in Figure 1 is considered. This idealized permeability field is characterized by a through-going, high-permeability layer (100 mD) embedded within a low-permeability layer (0.1 mD), both of which are orientated 20° from the vertical and imbedded within an intermediate-permeability matrix (10 mD). Two non-through-going, low-permeability features (0.1 mD) also appear isolated within the matrix.

Permeability tensors calculated for this field using the various upscaling techniques and boundary conditions are shown in Figure 2. The upscaled permeability tensors $\mathbf{k}^*$ for the domains shown in Figures 1a and 1c (red box) calculated using equation (3) and pressure–no-flow boundary conditions are both represented by the axis-aligned tensor shown in Figure 2a. Using equation (4) and mirror-periodic boundary conditions to model

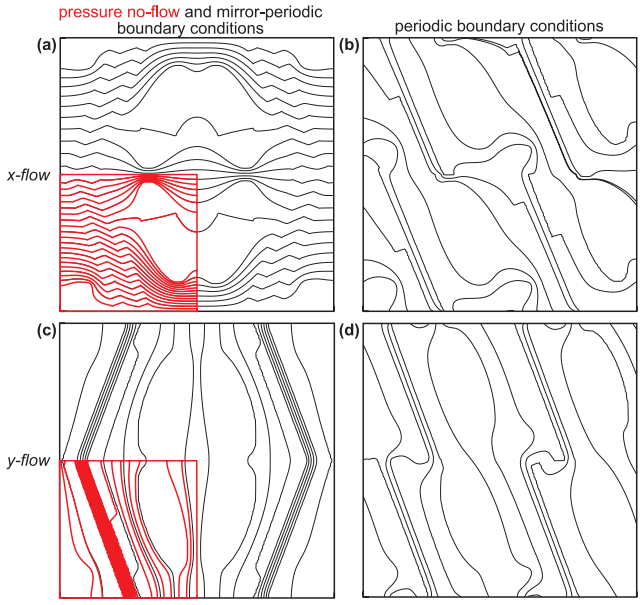

Fig. 3. Streamline maps for the permeability fields shown in Figure 1. Streamlines for pressure no-flow (red) and mirror-periodic boundary condition simulations for the (**a**) *x*- and (**c**) *y*-directions. Streamlines for periodic boundary condition simulations for the (**b**) *x*- and (**d**) *y*-directions.

flow over the entire mirrored domain shown in Figure 1c (red box) similarly leads to the tensor shown in Figure 2a. The symmetry of the mirror-periodic model results in a no-flow condition on the mirror boundaries which, in turn, yields the identical flow solution to that computed for the standard pressure–no-flow simulation. Furthermore, both the pressure–no-flow model and the mirror-periodic model computed over the target domain (Fig. 1c, blue box) using equation (4) (Fig. 2b) yield the same tensor. Because these two boundary conditions will always yield identical results, attention is focused only on pressure–no-flow conditions in subsequent discussions.

The $\mathbf{k}^*$ calculated using equation (4) and periodic boundary conditions yields a tensor with less contrast between the principal values than those calculated with the pressure–no-flow results (Fig. 2c). This is due to the fact that the highest and lowest permeability features are disrupted across the periodically reproduced domains (see Figure 1b), which results in the loss of connectivity of these important features. In the resulting calculation of $\mathbf{k}^*$ for this system, matrix flow dominates. These similarities and dissimilarities between boundary conditions are also reflected in the streamlines shown in Figure 3.

In light of the results presented above, it is useful to consider scenarios where one boundary condition would be more appropriate than the other. Two fracture geometries are shown in Figure 4, a left-stepping *en echelon* fracture set (left) and a single, through-going fracture (right). The fractures have high permeability (k_f) relative to the matrix (k_m). The paper considers upscaling these models to 3×3 grids, focusing on predicting global flow in the *y*-direction, Qy. Using pressure–no-flow boundary conditions for the local simulations, k^*_{yy} for the three central blocks reflects the high permeability of the fractures because each of the cells contains a locally through-going fracture (Fig. 4b) for either of the original fracture geometries. In the case of periodic boundary condition simulations, k^*_{yy} for the three central blocks reflects the low permeability of the matrix (Fig. 4c) because periodic repetition of the local domains disconnects the fractures, thereby reducing significantly the effects of high fracture permeability.

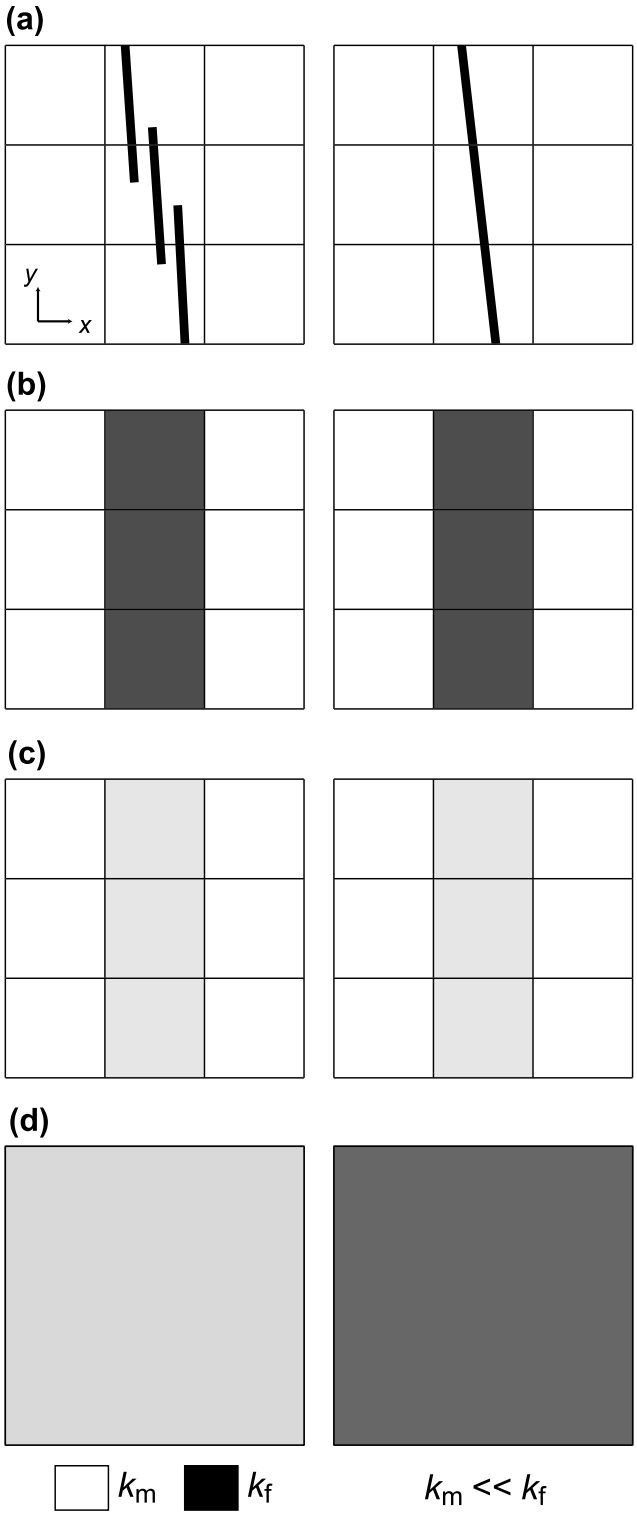

Fig. 4. Schematic example illustrating the effects of boundary conditions used to compute $\mathbf{k}^*$. Dark colours indicate high permeability, while light colours indicate low permeability. (**a**) *En echelon* stepping fractures (left) and a single, through-going fracture (right). (**b**) 3×3 vertical upscaling using pressure–no-flow boundary conditions. (**c**) 3×3 vertical upscaling using periodic boundary conditions. (**d**) Global Qy for both domains.

The global flow, Qy, for the *en echelon* fracture geometry should reflect the low-permeability matrix due to the disconnected nature of the fractures and the lack of communication between them. By contrast, Qy for the through-going fracture

model should reflect the permeability of the fracture itself. Periodic boundary conditions are therefore more appropriate for naturally disconnected fracture geometries or for connected geometries where the local domain is chosen such that connectivity is preserved, while the pressure–no-flow boundary conditions are more appropriate for through-going fracture geometries (Fig. 4d). This demonstrates that the appropriateness of a local boundary condition depends on the larger-scale connectivity of the dominant fault zone features. In the next section, the effects of boundary conditions on upscaled quantities are further explored by examining permeability fields that occur in the vicinity of a fault zone.

APPLICATION TO FAULT ZONE UPSCALING

The faults studied were formed by shearing along pre-existing joint zones in the Aztec sandstone located in the Valley of Fire State Park, southern Nevada. The details of this faulting style are discussed by Myers (1999), Davatzes & Aydin (2003) and Flodin & Aydin (2004). In subsequent calculations attention is focused on an outcrop map of a portion of a fault with about 14 m of left-lateral slip (Fig. 5).

The fault shown in Figure 5 consists of five structural elements, each of which exhibits a characteristic permeability. The elements are joints, sheared joints, deformation bands, fault rock and slip surfaces, all of which are embedded within undeformed host rock. Assignment of permeability to each of the elements is discussed by Myers (1999) and Jourde *et al.* (2002). Here, representative values are applied to each of the fault elements. Fault rock, sheared joints and deformation bands are assigned a permeability of 0.1 mD. Permeability for joints and slip surfaces are calculated using a parallel-plate model with an aperture of 0.25 mm. Finally, host rock is assigned a permeability of 200 mD.

Three regions were chosen from the fault zone shown in Figure 5a for further investigation. For each of the three regions, three upscaling methods are evaluated: (1) pressure–no-flow, with $\mathbf{k}^*$ computed from the outlet average (no-flow outlet); (2) pressure–no-flow, with $\mathbf{k}^*$ computed from the area average (no-flow area); and (3) periodic boundary conditions. The first region is extracted from the fault damage zone (Fig. 5a) and is characterized by the occurrence of variably orientated structural elements (joints and sheared joints) that do not form a connected network at the larger scale (Fig. 5b). Results for the simulations of this permeability field using the three different boundary conditions are presented in Table 1. Principal values of permeability calculated using no-flow (with area averaging) and periodic boundary conditions are in qualitative agreement. The no-flow outlet result deviates from the other two results because the cross-terms are implicitly assumed to be zero. As such, this result does not reflect the 26–30° orientation of $\mathbf{k}^*$. The periodic and no-flow area results are in fair agreement because the permeability field in this case lacks dominant through-going features.

The second region is from an area selected from the fault core (Fig. 5a) and is characterized by a through-going low-permeability fault rock zone with associated through-going high-permeability slip surfaces (Fig. 5c). In the immediate periphery of the fault rock is a dense network of joints, sheared joints and deformation bands. No-flow area and no-flow outlet calculations of k_1 yield nearly identical results, while the periodic boundary condition result is over a factor of two less than the no-flow calculations (Table 1). In all three cases, nearly all of the flow in the k_1 direction is focused along the through-going slip surfaces, a high-permeability pathway. For the k_2 direction, all methods yield the same results because of

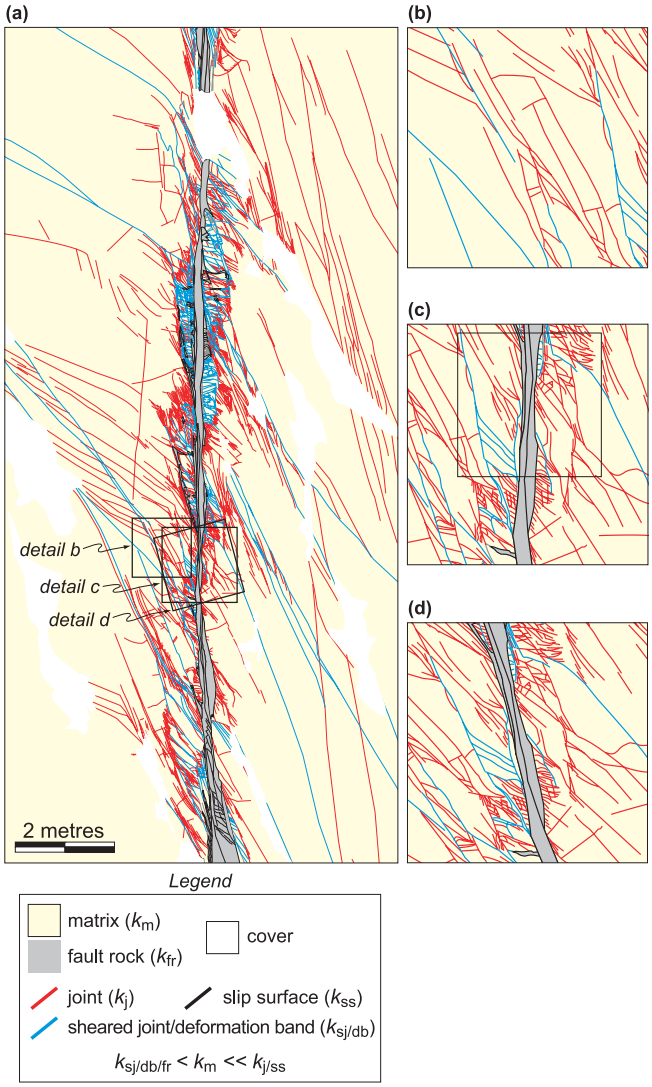

Fig. 5. (**a**) Map of a sheared joint fault with 14 m left-lateral offset (after Myers 1999). (**b**) Sub-region chosen from the fault damage zone. Model dimensions are 400 × 400. (**c**) Sub-region chosen from the fault core. Inset black box is the region shown in Figure 7a. Model dimensions are 500 × 500. (**d**) 15° counterclockwise-rotated version of the sub-region shown in (c). Model dimensions are 500 × 500.

the presence of the through-going low-permeability fault rock. Because the two dominant low and high-permeability features are aligned with the *y*-axis, the cross-terms are negligible and the principal directions of $\mathbf{k}^*$ are aligned with the coordinate system (Table 1). This explains the close agreement between the no-flow outlet and no-flow area results. For this case, the calculation with periodic boundary conditions gives lower values for k_1 because the large-scale connectivity is not maintained due to mismatches at the domain boundary.

The third region is a 15° counterclockwise-rotated version of approximately the same fault core region used in the second example (Fig. 5a). This example (detailed in Figure 5d) shows the greatest difference in results between the no-flow and periodic boundary condition simulations. The principal permeabilities for both no-flow methods are in relatively good agreement, although the no-flow outlet result does not recover the 15° counterclockwise rotation of the model domain (Table 1). Compared to the no-flow results, k_1 for the periodic boundary condition result is nearly a factor of two less, while k_2

Table 1. *Upscaling results for the maps shown in Figures 5b–c.*

Input map	Boundary condition	Principal permeability		
		k_1	k_2	θ
Fault damage	no-flow outlet	1026.4	210.5	—
zone (Fig. 5b)	no-flow area	1708.8	154.0	26.8
	periodic	1250.6	184.1	30.0
Fault core	no-flow outlet	4274.8	4.9	—
(Fig. 5c)	no-flow area	4267.7	4.9	−0.29
	periodic	1740.1	4.9	0.22
Fault core – 15°	no-flow outlet	3552.1	5.5	—
counterclockwise	no-flow area	4298.9	4.5	14.7
	periodic	2309.7	229.6	32.9

is more than an order of magnitude greater. This is due to the fact that, in the periodic domain, the low-permeability fault rock no longer forms a lateral barrier and flow is allowed a window through the fault core. Also, the presence of a high concentration of joints on the top right side of the fault (red lines in Fig. 5d) appears to juxtapose the damage zone between the fault core in the original and the periodically imaged block. This leads to the anomalously high k_2 value and the greater rotation of the principal directions.

POWER AVERAGING METHODS

Before describing the partial upscaling approach for improving the accuracy of coarse-scale models of the fault zone, the application of power averaging techniques (Deutsch 1989) for the representation of fault zone permeability is briefly considered. The use of power averaging methods to estimate upscaled permeability of a fault zone containing joints (volume fraction V_j and permeability k_j), fault rock (volume fraction V_{fr} and permeability k_{fr}) and host rock (volume fraction V_h and permeability k_h) was first considered by Myers (1999). The upscaled permeability is computed via:

$$k_i^* = (V_j k_j^{\omega_i} + V_{fr} k_{fr}^{\omega_i} + V_h k_h^{\omega_i})^{1/\omega_i}, \quad (5)$$

where k_i^* is the upscaled permeability in the direction i (i=x, y) and ω_i is the power averaging exponent (which can vary with direction).

The power averaging exponent is generally determined by tuning to numerical results (e.g. Flodin *et al.* 2001). This study attempted to tune ω_i to reproduce $\mathbf{k}^*$ computed in the previous section. Accurate results were difficult to achieve, however, because equation (5) is unable to distinguish between connected and disconnected features of the type shown in Figure 4. Consider, for example, two models that have the same fraction of joints, fault rock and host rock, with one model containing large-scale joint connectivity while the other one does not. Equation (5) cannot capture this important distinction because both models have the same volume fractions of the various structural components. This limits the applicability of the power averaging procedure for models of this type. This restriction limitation is somewhat analogous to the variation in $\mathbf{k}^*$ with boundary conditions illustrated in the previous section.

Rather than use a power averaging procedure to estimate $\mathbf{k}^*$ for small regions of the fault zone, its applicability for estimating large-scale fault zone permeability is illustrated. Data for the 14 m slip fault example (Fig. 5) are supplemented with additional data for a smaller fault with 6 m and a larger fault with 150 m of slip that were described by Myers (1999). As indicated previously, Jourde *et al.* (2002) computed the upscaled fault zone permeabilities for these models using pressure–no-flow boundary conditions and outlet averaging. In these systems, the large-scale fault zone permeability is nearly aligned with the fault orientation. Therefore, the principal values of $\mathbf{k}^*$ provide fault-parallel and fault-normal permeabilities.

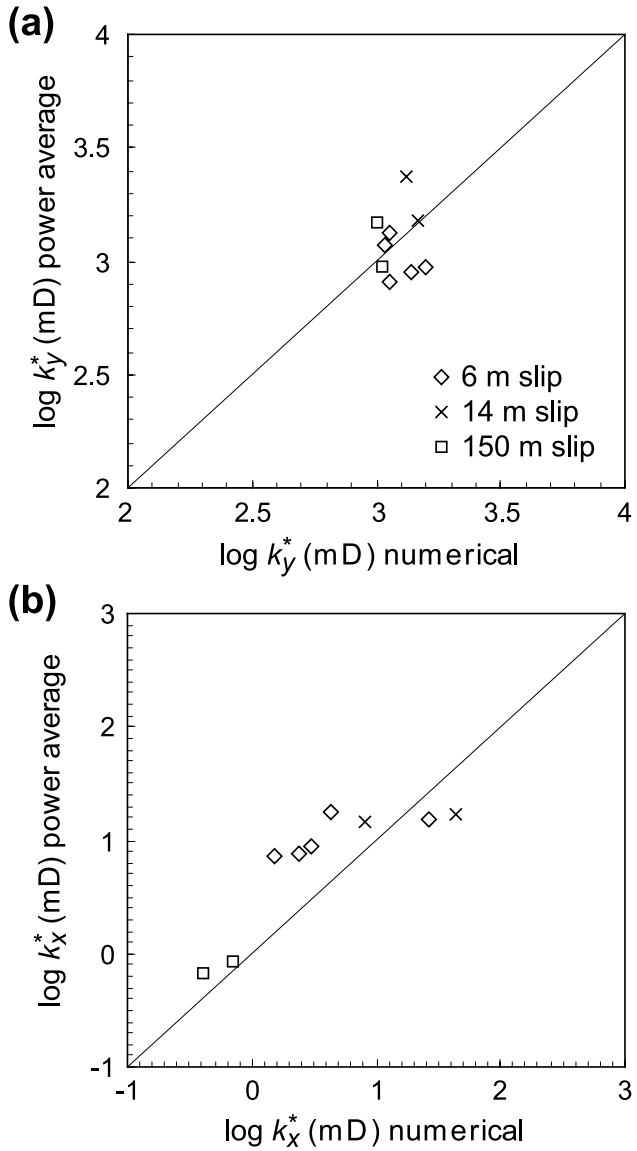

Fig. 6. Comparison of power average and numerical simulation upscaling results for (**a**) along-fault and (**b**) cross-fault permeability.

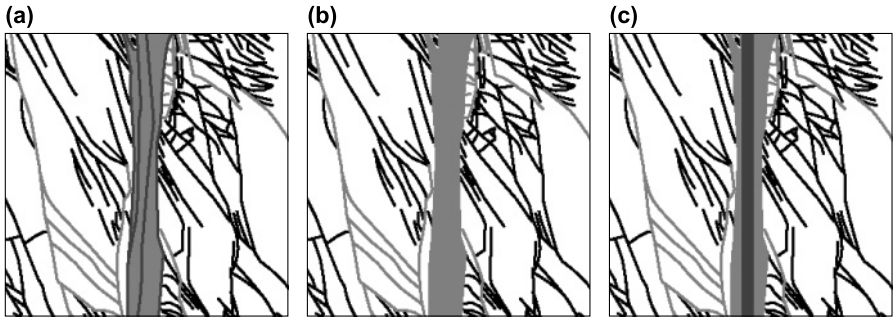

Fig. 7. (**a**) Sub-region of the fault core shown in Figure 5c. (**b**) The same region shown in (a) without the through-going slip surfaces. (**c**) The same region shown in (b) with a uniform 13-pixel wide slip surface added. All regions have model dimensions 300×300.

For the fault parallel direction (k_y^*), flow is dominated by connected high-permeability features. For all of the fault data, a value of ω_y=0.61 provided the best correspondence between numerical and power averaging results for along-fault flow (Fig. 6a). The data are, however, clustered over a relatively small range, so one cannot assess the limits of applicability of this ω_y. For flow in the fault perpendicular direction (k_x^*), results are dominated by the presence of low-permeability fault rock. In this case, a value of $\omega_x = -0.53$ provided the best correspondence between numerical and power averaging results (Fig. 6b). Although numerical results can be expected to provide better accuracy, these power average estimates for $\mathbf{k}^*$ might be adequate for some applications.

EXPLICIT FRACTURE MODELLING

The results from the section on 'Application to fault zone upscaling' illustrate that the upscaled permeabilities of fault zones can be highly dependent on the boundary conditions used for the $\mathbf{k}^*$ calculation. These ambiguities result when one tries to 'homogenize' dominant through-going features. This sensitivity to boundary conditions is, perhaps, not surprising since homogenization theory, on which many upscaling procedures are based, requires that the relevant heterogeneities be small relative to the size of the upscaled region. This requirement is clearly violated in the models presented here. For this reason, the notion of explicitly representing the dominant through-going high-permeability features in otherwise upscaled fault permeability models is now explored.

This 'partial upscaling' procedure is as follows. First, the high-permeability, connected and through-going features are removed from the fine-scale fault permeability field. In practice, these features could be identified through preprocessing of the fine-scale data using a single phase flow calculation (analogous to the identification of high flow regions in Durlofsky *et al.* 1997) or via a consideration of the connectivity of the fracture network (e.g. Jing & Stephansson 1997). Following extraction of the through-going features, the rest of the model is upscaled to a coarse grid. Finally, the high-permeability features are reintroduced back into the coarsened model.

This approach shares some similarities with previous techniques. For example, Lee *et al.* (2001), in their modelling of flow in fractured reservoirs, introduced a three-step methodology. They first derived an analytical solution to account for the permeability influence of the shortest fractures and then applied a numerical boundary element method to upscale the medium-length fractures. Finally, they then explicitly modelled the longest fractures within the background permeability field obtained in the previous two steps. The methodology here differs from that in Lee *et al.* (2001) in that our study explicitly models the slip surfaces using fine grids within the coarsened model, similar to the non-uniform coarsening approach of Durlofsky *et al.* (1997). Lee *et al.* (2001), by contrast, represented the large fractures using a treatment analogous to that applied for the modelling of wells in finite-difference procedures.

The methodology is now applied to an example fault zone and the accuracy tested by comparing global flow-rates and oil cut (fraction of oil in the produced fluid) between a fine-scale model and the upscaled models. The case is considered where the *in situ* fluid (oil) and the injected fluid (water) have the same viscosity and the relative permeability of each phase is linear in the phase saturation. These simplifications result in a system in which the global flow-rate does not change in time. In addition, the breakthrough behavior of the injected fluid and, thus, the oil cut, can be readily calculated from the global pressure solution. See Durlofsky *et al.* (1997) for a detailed description of these calculations.

A 300×300 cell sub-region selected from the fault map shown in Figure 5c is considered (Fig. 7a). In the first step, the through-going slip surfaces are removed from the fine-scale fault map (Fig. 7b) and then upscaled to a coarse grid. For the local upscaling problem, no-flow boundary conditions are used and $\mathbf{k}^*$ is computed using the outlet average. To test the robustness of the upscaling, four different grid coarsenings are applied: 50×50, 30×30, 10×10 and 3×3. The resulting upscaled permeability fields are shown in Figures 8a–d. Finally, a single, uniform slip surface is reintroduced to the central portion of the upscaled models.

The properties and dimensions of the uniform slip surface are calibrated to the original fine-scale model. This is accomplished by matching global flow-rates between the original fine-scale model and the modified fine-scale model with the single uniform slip surface (Fig. 7c, Table 2). Replacing the original slip surfaces with the uniform slip surface in the fine-scale model is done simply for numerical convenience. Specifically, the finite-difference code applied in this study uses Cartesian grids, so slip surfaces not aligned with a coordinate direction could not be accurately modelled on coarse grids. The uniform slip surface in the modified fine model is, therefore, aligned with the *y*-axis. Note that this step might not be necessary if one applies unstructured grid techniques or a general nine-point finite-difference method capable of accurately treating non-orthogonal grid effects.

Comparisons of global flow results between the variously upscaled models (with the reintroduced uniform slip surface) are shown in Table 2. Flow rates in the *y*-direction are in fair agreement (all within 18% of the fine-grid result; see Table 2) between all of the tested models. However, for flow in the *x*-direction, the upscaled models differ from the fine model by as much as 50%. In the 50×50 case, the *x*-flow was overestimated, while in the other cases it was underestimated (Table 2). These discrepancies are likely to be due to permeability changes in the fault periphery of the upscaled models. In the coarser models (30×30 and coarser), high flow features that were locally continuous in the fine model were rendered discontinuous in the coarsened model, resulting in lower values of Q_x.

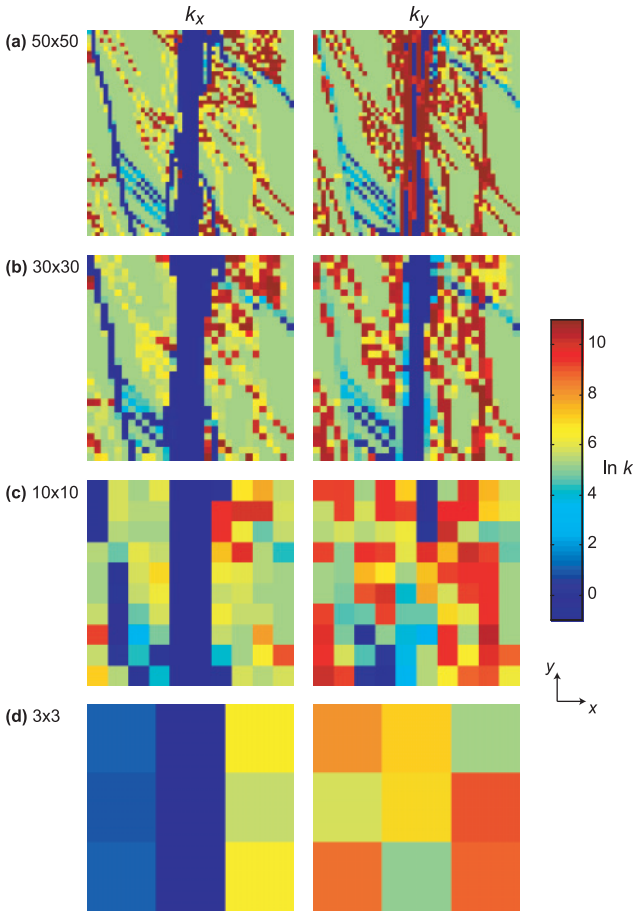

Fig. 8. Upscaling results for coarse models of different dimensions using local pressure–no-flow boundary conditions and the input map shown in Figure 7b (slip surfaces removed).

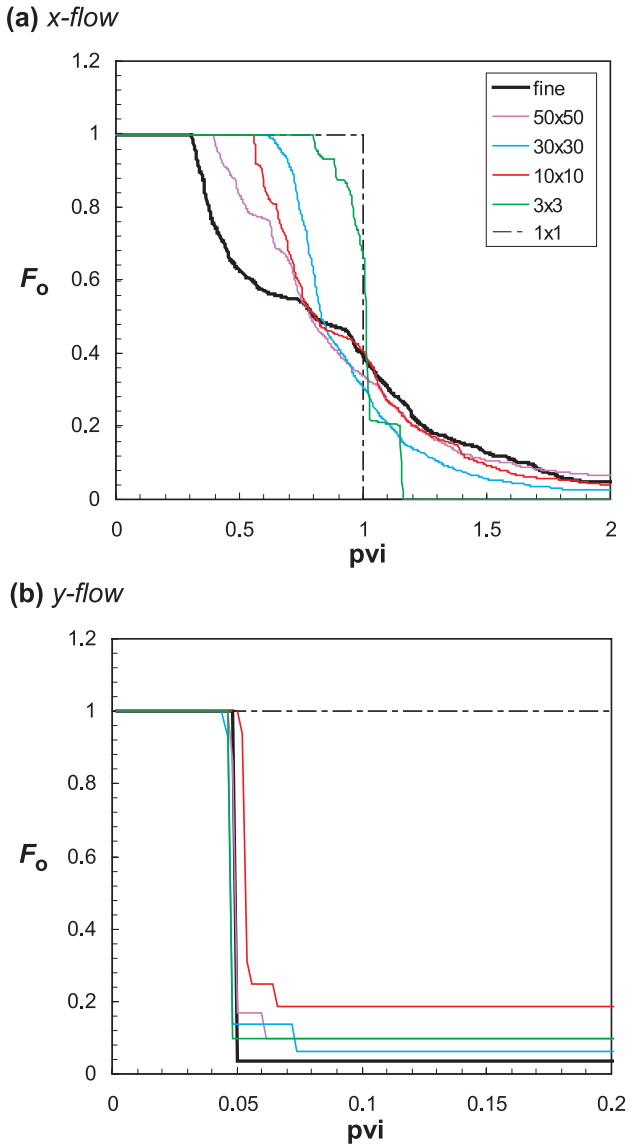

Fig. 9. Oil cut (F_o) versus pore volume injected (pvi) at the outlet edge for (**a**) cross-fault and (**b**) along-fault flow. Uniform slip surface reintroduced to all models.

In the 50×50 model, by contrast, continuity of high-permeability features was enhanced.

To test the transport properties of the upscaled models, the study simulates the outlet oil cut (F_o) in an oil–water system, as a function of pore volume injected (pvi=Qt/V_p, where t is time and V_p is the total pore volume of the system). As indicated above, it is assumed that oil and water have the same viscosity and that the relative permeability of each phase is linear in the phase saturation. For flow in the x-direction (fault-perpendicular flow), the finer upscaled models match more closely the flow behaviour of the original model (Fig. 9a). This is likely to be due to the increasing loss of connection of high-permeability joints in the fault periphery (cf. Fig. 5a) with increasing coarsening, which was similarly noted in the global flow calculations.

All of the upscaled models adequately reproduced the initial breakthrough behaviour of the fine-scale models for flow in the y-direction (fault-parallel flow), as illustrated in Figure 9b. Note that this breakthrough occurs at a very early time (*c.* 0.05 pvi). Also shown on the fractional flow curves is the result for a 1×1 globally upscaled region. In this case, the permeability is homogeneous and breakthrough occurs at 1 pvi. This indicates that, although the total flow-rate can be adequately matched using a single global value for $\mathbf{k}^*$, the transport behaviour cannot. However, as indicated by the above results, the

Table 2. *Global flow characteristics for the permeability field shown in Figures 7a, 7c and 8a–d*

Input model	Dimension	Global	
		Qx	Qy
Original with uniSS (Fig. 6c)	300×300	1.16	6574.9
Coarsened model (Fig. 7a) with added uniSS	50×50	1.74	7025.7
Coarsened model (Fig. 7b) with added uniSS	30×30	0.90	6777.1
Coarsened model (Fig. 7c) with added uniSS	10×10	0.85	7766.1
Coarsened model (Fig. 7d) with added uniSS	3×3	0.76	7016.2

uniSS, uniform slip surface.

transport properties can be greatly improved through the reintroduction of the slip surfaces, even when the model is otherwise very coarse.

The two-step partial upscaling–explicit fracture modelling approach presented here can be extended in a number of useful directions. Most notably, it can be coupled with recent discrete fracture modelling techniques that utilize unstructured grids (e.g. Granet *et al.* 2001; Karimi-Fard *et al.* 2003) to provide a highly efficient and general overall model.

CONCLUSIONS

In this paper, different approaches for upscaling detailed descriptions of fault zones were investigated. In particular, the effects of the choice of boundary conditions and post-processing procedure were focused upon. A partial upscaling technique for including the effects of high-permeability, through-going features in coarsened models was also described. A number of conclusions can be drawn from this work.

1. The choice of pressure–no-flow, periodic and mirror-periodic boundary conditions applied to fault permeability upscaling was shown to influence the calculated results in many cases. Pressure–no-flow conditions are more appropriate for capturing the effects of large-scale through-going fractures, while periodic boundary conditions are more applicable for disconnected fracture geometries.
2. Power averaging procedures were tuned to capture large-scale fault-parallel and fault-normal permeabilities. The power averaging approach was found to be less suitable for the calculation of smaller-scale grid block permeabilities.
3. A partial upscaling technique, in which high-permeability through-going features (e.g. slip surfaces) were modelled explicitly and the remainder of the system was upscaled, was shown to be well suited for the coarse-scale representation of the fault zone. Using this approach, the coarse model is able to predict both total flow-rate as well as transport behaviour (e.g. oil cut).

We are grateful to Xian-Huan Wen at ChevronTexaco Energy Technology Company for providing us with the numerical upscaling code as well as support for its use. Discussions with Rod Myers are appreciated. This work was supported in part by the Rock Fracture Project at Stanford University and a grant from the US Department of Energy, Office of Basic Energy Sciences (DE-FG03-94ER14462) (to Atilla Aydin and David D. Pollard).

REFERENCES

Caine, J.S. & Forster, C.B. 1999. Fault zone architecture and fluid flow: Insights from field data and numerical modelling. *In:* Haneberg, W.C. (ed.) *Faults and subsurface fluid flow in the shallow crust*. Geophysical Monograph, **113**. American Geophysical Union, 101–127.

Chen, Y., Durlofsky, L.J., Gerritsen, M. & Wen, X.H. 2003. A coupled local–global upscaling approach for simulating flow in highly heterogeneous formations. *Advances in Water Resources,* **26**, 1041–1060.

Couples, G. D., Lewis, H., Reynolds, M. A. et al. 2003. Upscaling fluid-flow and geomechanical properties in coupled matrix+fractures+fluids systems. Paper SPE 79696, presented at the SPE Reservoir Simulation Symposium, Houston, 3–5 February.

Davatzes, N.C. & Aydin, A. 2003. The formation of conjugate normal fault systems in folded sandstone by sequential jointing and shearing, Water Pocket monocline, Utah. *Journal of Geophysical Research,* **108**(B10), 2478–2493.

Deutsch, C. 1989. Calculating effective absolute permeability in sandstone/shale sequences. *SPE Formation Evaluation,* **4**, 343–348.

Durlofsky, L.J. 1991. Numerical calculation of equivalent grid block permeability tensors for heterogeneous porous media. *Water Resources Research,* **27**, 699–708.

Durlofsky, L.J., Jones, R.C. & Milliken, W.J. 1997. A nonuniform coarsening approach for the scale-up of displacement processes in heterogeneous media. *Advances in Water Resources,* **20**, 335–347.

Flodin, E.A. & Aydin, A. 2004. Evolution of a strike-slip fault network, Valley of Fire, southern Nevada. *Geological Society of America Bulletin,* **116**, 42–59.

Flodin, E. A., Aydin, A., Durlofsky, L. J. & Yeten, B. 2001. Representation of fault zone permeability in reservoir flow models. Paper SPE 71671, presented at the SPE Annual Technical Conference and Exhibition, New Orleans, 30 September– 3 October.

Granet, S., Fabrie, P., Lemonnier, P. & Quintard, M. 2001. A two-phase flow simulation of a fractured reservoir using a new fissure element method. *Journal of Petroleum Science and Engineering,* **32**, 35–52.

Harris, D., Yielding, G., Levine, P., Maxwell, G., Rose, P.T. & Nell, P. 2002. Using Shale Gouge Ratio (SGR) to model faults as transmissibility barriers in reservoirs: an example from the Strathspey Field, North Sea. *Petroleum Geoscience,* **8**, 167–176.

Holden, L. & Nielsen, B.F. 2000. Global upscaling of permeability in heterogeneous reservoirs: The Output Least Squares (OLS) method. *Transport in Porous Media,* **40**, 115–143.

Jing, L. & Stephansson, O. 1997. Network topology and homogenization of fractured rocks. *In:* Jamtveit, B. & Yardley, B.W.D. (eds) *Fluid flow and transport in rocks*. Chapman & Hall, London, 191–202.

Jourde, H., Flodin, E.A., Aydin, A., Durlofsky, L.J. & Wen, X.-H. 2002. Computing permeability of fault zones in aeolian sandstone from outcrop measurements. *AAPG Bulletin,* **86**, 1187–1200.

Karimi-Fard, M., Durlofsky, L. J. & Aziz, K. 2003. An efficient discrete fracture model applicable for general purpose reservoir simulators. Paper SPE 79699, presented at the SPE Reservoir Simulation Symposium, Houston, 3–5 February.

Lee, S.H., Lough, M.F. & Jensen, C.L. 2001. Hierarchical modeling of flow in naturally fractured formations with multiple length scales. *Water Resources Research,* **37**, 443–455.

Manzocchi, T., Walsh, J.J., Nell, P. & Yielding, G. 1999. Fault transmissibility multipliers for flow simulation models. *Petroleum Geoscience,* **5**, 53–63.

Manzocchi, T., Heath, A.E., Walsh, J.J. & Childs, C. 2002. The representation of two phase fault-rock properties in flow simulation models. *Petroleum Geoscience,* **8**, 119–132.

Martys, N.S., Hagedorn, J.G., Goujon, D. & Devaney, J.E. 1999. Large-scale simulations of single and multi-component flow in porous media. *The International Society for Optical Engineering (SPIE),* **3772**, 205–213.

Myers, R.D. 1999. *Structure and hydraulics of brittle faults in sandstone*. PhD thesis. Stanford University, Stanford, CA.

Myers, R.D. & Aydin, A. 2004. The evolution of faults formed by shearing across joint zones in sandstone. *Journal of Structural Geology,* **26**, 947–966.

Nakashima, T., Sato, K., Arihara, N. & Yazawa, N. 2000. Effective permeability estimation for simulation of naturally fractured reservoirs. Paper SPE 64286, presented at the SPE Asia Pacific Oil and Gas Conference and Exhibition, Brisbane, Australia, 16–18 October.

Pickup, G.E., Ringrose, P.S., Jensen, J.L. & Sorbie, K.S. 1994. Permeability tensors for sedimentary structures. *Mathematical Geology,* **26**, 227–250.

Renard, Ph. & de Marsily, G. 1997. Calculating equivalent permeability: A review. *Advances in Water Resources,* **20**, 253–278.

Shipton, Z.K., Evans, J.P., Robeson, K.R., Forster, C.B. & Snelgrove, S. 2002. Structural heterogeneity and permeability in faulted eolian sandstone: Implications for subsurface modeling of faults. *AAPG Bulletin,* **86**, 863–883.

Walsh, J.J., Watterson, J., Heath, A.E. & Childs, C. 1998. Representation and scaling of faults in fluid flow models. *Petroleum Geoscience,* **4**, 241–251.

Wen, X.-H. & Gomez-Hernandez, J.J. 1996. Upscaling hydraulic conductivities in heterogeneous media: An overview. *Journal of Hydrology,* **183**, ix–xxxii.

Wen, X.-H., Durlofsky, L.J. & Edwards, M.G. 2003. Use of border regions for improved permeability upscaling. *Mathematical Geology,* **35**, 521–547.

Wu, X.H., Efendiev, Y. & Hou, T.Y. 2002. Analysis of upscaling absolute permeability. *Discrete and Continuous Dynamical Systems – Series B,* **2**, 185–204.

Received 7 May 2003; revised typescript accepted 3 October 2003.